Published in final edited form as:
Chem. 2024 February 08; 10(2): 675–685. doi:10.1016/j.chempr.2023.11.002.

Controlled catalyst-transfer polymerization in graphene nanoribbon synthesis

Sai Ho Pun[1,5], **Aidan Delgado**[1,5], **Christina Dadich**[1,5], **Adam Cronin**[1], **Felix Raoul Fischer**[1,2,3,4,6,*]

[1]Department of Chemistry, University of California, Berkeley, Berkeley, CA 94720, USA

[2]Materials Sciences Division, Lawrence Berkeley National Laboratory, Berkeley, CA 94720, USA

[3]Kavli Energy NanoScience Institute at the University of California Berkeley and the Lawrence Berkeley National Laboratory, Berkeley, CA 94720, USA

[4]Bakar Institute of Digital Materials for the Planet, Division of Computing, Data Science, and Society, University of California, Berkeley, Berkeley, CA 94720, USA

[5]These authors contributed equally

[6]Lead contact

SUMMARY

Exercising direct control over the unusual electronic structures arising from quantum confinement effects in graphene nanoribbons (GNRs) is intimately linked to geometric boundary conditions imposed by the structure of the ribbon. Besides composition and position of substitutional dopant atoms, the symmetry of the unit cell, width, length, and termination of a GNR govern its electronic structure. Here, we present a rational design that integrates each of these interdependent variables within a modular bottom-up synthesis. Our hybrid chemical approach relies on a catalyst-transfer polymerization that establishes excellent control over length, width, and end groups. Complemented by a surface-assisted cyclodehydrogenation step, uniquely enabled by matrix-assisted direct (MAD) transfer protocols, geometry and functional handles encoded in a polymer template are faithfully mapped onto the structure of the corresponding GNR. Bond-resolved scanning tunneling microscopy (BRSTM) and spectroscopy (STS) validate the robust correlation between polymer template design and GNR electronic structure.

---

[*]Correspondence: ffischer@berkeley.edu.

AUTHOR CONTRIBUTIONS
S.H.P., A.D., C.D., and F.R.F. initiated and conceived the research; S.H.P. and C.D. designed, synthesized, and characterized monomer, catalyst, and polymer; A.D. and A.C. performed on-surface synthesis, STM characterization, and data analysis. S.H.P, C.D., A.D., and F.R.F. wrote the manuscript. All authors contributed to the scientific discussion. S.H.P., A.D., and C.D. contributed equally.

DECLARATION OF INTERESTS
The authors declare no competing interests.

INCLUSION AND DIVERSITY
We support inclusive, diverse, and equitable conduct of research.

SUPPLEMENTAL INFORMATION
Supplemental information can be found online at https://doi.org/10.1016/j.chempr.2023.11.002.

Graphical Abstract

This study describes a hybrid strategy for bottom-up synthesizing graphene nanoribbons (GNRs) that provides exquisite control over the length, width, and functional end groups. The combination of solution-based Suzuki chain transfer polymerization (SCTP) with on-surface synthesis enabled by matrix-assisted direct (MAD) transfer presents an unparalleled tool to access and fine-tune all critical parameters that define the electronic band structure of GNRs. This technology paves the way for advancements in the field of carbon-based nanoelectronics sensing and computing.

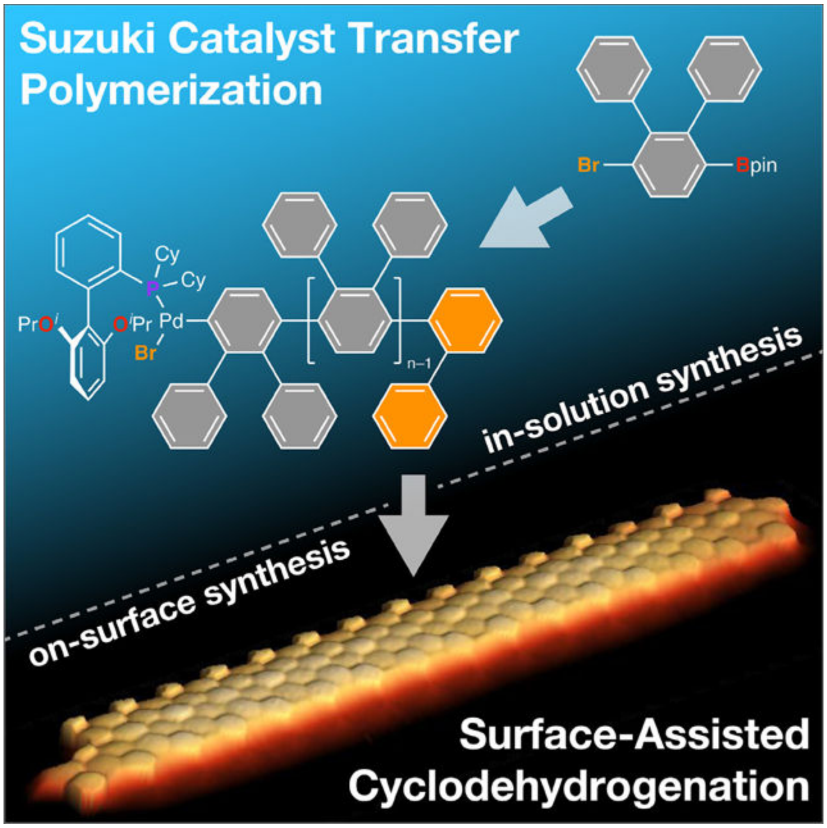

INTRODUCTION

The chemical bottom-up synthesis of atomically defined graphene nanoribbons (GNRs) from molecular building blocks, either in solution or on surfaces, has dominated attempts to control integral structural parameters such as crystallographic symmetry, width, density, and position of dopant atoms. Although step-growth polymerizations[1] based on Diels-Alder cycloaddition[2–4] or transition metal-catalyzed Suzuki-Miyaura[5–9] and Yamamoto[10,11] cross-coupling reactions have advanced solution-based approaches, the on-surface synthesis (OSS) of GNRs has largely relied on radical step-growth mechanisms.[12–15] Neither of these techniques has been able to demonstrate uncompromising coextensive control over polymer sequence, length, and termination underpinning structural parameters that define the electronic structure of GNRs. Although iterative cross-coupling deprotection sequences have been used to access uniform samples of oligomeric GNRs,[9] a stepwise linear synthesis approach cannot be scaled beyond modest ribbon lengths. Although the design of the molecular building block used in solution- and surface-based polymerizations has customarily served to establish symmetry, width, and substitutional dopant levels, precise control over the length and functional termination of GNRs remains a veritable challenge and represents an indispensable stepping stone toward the successful integration of functional GNRs with advanced electronic circuit architectures and sensing nanotechnology.

Our strategy to exercise unprecedented length control and chemical functionalization of solution-synthesized GNR precursors builds on recent advancements in Suzuki catalyst-transfer polymerization (SCTP) reactions.[16–26] Herein, a bifunctional monomer (**M**), e.g., the *o*-terphenylenes **1a**,**b** (Figure 1A) featuring orthogonal functional groups, a halide (Br) and a boronic ester (Bpin) placed at the *para* positions of a central phenyl ring defining the axis of polymerization, is linearly extended into a one-dimensional (1D) polymer chain under the action of a palladium cross-coupling catalyst. A distinguishing feature of this class of polymerizations is that the Pd catalyst, following the reductive elimination step, does not dissociate from the growing polymer chain. Instead, it remains coordinated to the **π**-system and migrates across the last aromatic ring in the polymer chain before reinserting into the C–Br bond priming the propagating catalyst for successive transmetalation with an arylboronate ester.[27,28] We envisioned that a preformed aryl-halide Pd-complex (e.g., 2 in Figure 1A) could serve as a competent initiator (I) and catalyst for SCTP of *o*-terphenylenes 1a,b. The initiation step reliably transfers a functional end-group (e.g., the biphenyl highlighted in blue) to the inactive end of the growing polymer chain. In the absence of competing chain transfer (k_{ct}) and chain termination (k_t) steps, a fast initiation (k_i) and a near-constant rate of propagation (k_p) ensures that the degree of polymerization (*DP*), and consequently, the final length of the resulting polymers, can be controlled by the $[M]_0/[I]_0$ loading if $k_i > k_p \gg k_{ct} \sim k_t$. Once all monomers have been consumed, the reactive chain ends can be terminated by coupling to a monofunctional terminator (T) (e.g., the phenylboronic acid 3 highlighted in orange) that caps the polymer chain and irreversibly dissociates the Pd catalyst. The resultant 1D polymers not only feature narrowly defined length distributions but two chemically distinct and individually addressable functional handles at either end of the polymer chain that map directly onto the structure of the corresponding N = 9 armchair GNRs (9-AGNRs, N is the number of C-atoms counted across the width of the ribbon).

RESULTS AND DISCUSSION

Controlled living Suzuki catalyst-transfer polymerization

A broad catalyst screening established the optimal conditions for a controlled living SCTP. The *o*-terphenylene monomer **1a** ($R^1 = H$) polymerizes readily under the action of a preformed Pd(RuPhos) aryl bromide catalyst **2**, in the presence of an aqueous base (K_3PO_4) in tetrahydrofuran (THF) at 24°C to give the characteristic *p*-phenylene backbone of *poly*-**1a** (Figure 1A). Size exclusion chromatography (SEC) calibrated to polystyrene (PS) standards reveals monomodal distributions with low dispersity ($Đ = 1.19$) at low $[\mathbf{M}]_0/[\mathbf{I}]_0 < 20$ that broaden at higher loadings as the solubility of the growing polymer chains decreases abruptly (Figure S1). Polymers resulting from the reaction of *o*-terphenylene monomer **1b** ($R^1 = C_{12}H_{25}$) with **2** instead remain soluble in the reaction mixture at $[\mathbf{M}]_0/[\mathbf{I}]_0$ loadings of up to 100. Even after the consumption of all monomers, the propagating catalyst species attached to the end of the growing polymer chain remains active and readily reacts with phenylboronic acid **3**, used here as a monofunctional chain-terminating agent. The resulting number-average molecular weight (M_n), dispersity (Đ = M_w/M_n; M_w is the weight average molecular weight), *DP*, average polymer length $\left(\bar{l}\right)$, termination efficiency, and isolated polymer yield at various $[\mathbf{M}]_0/[\mathbf{I}]_0$ loadings are summarized in Figure 1B. SEC traces of crude *poly*-**1b** samples prepared by SCTP show monomodal distributions (Figure 1C). The M_n increases linearly with the $[\mathbf{M}]_0/[\mathbf{I}]_0$ loading from $M_n = 7.8 \times 10^3$ g mol^{-1} ($[\mathbf{M}]_0/[\mathbf{I}]_0$ = 20) to $M_n = 52.9 \times 10^3$ g mol^{-1} ($[\mathbf{M}]_0/[\mathbf{I}]_0$ = 100), whereas the dispersity remains low (Đ % 1.2) (Figure 1D). SEC samples of *poly*-**1b** taken at different timepoints from a SCTP reaction ($[\mathbf{M}]_0/[\mathbf{I}]_0$ = 25) reveal a linear correlation between M_n and the monomer conversion, indicative of a living chain-growth mechanism (Figure 1E). MALDI-TOF mass spectrometry of *poly*-**1b** samples shows a characteristic family of peaks separated by the monomer repeat unit $\Delta m/z = 564.8 \pm 2.8$ (Figure 1F). The mass of the detected molecular ions $[\mathrm{M}]^+$ = [*poly*-1b–CHO] corresponds to the terminated polymers and spans from $5 < DP < 24$ for $[\mathbf{M}]_0/[\mathbf{I}]_0$ = 20. Despite the loss of the labile aldehyde group during ionization, matrix-assisted laser desorption ionization time-of-flight (MALDI-TOF) mass spectrometry supports the formation of telechelic polymers featuring both chemically unique end groups transferred as part of initiation and termination steps. ^{1}H NMR spectrum of *poly*-**1b** shows two characteristic resonance peaks at $\delta = 3.27$ ppm and $\delta = 9.88$ ppm corresponding to the dimethyl acetal and the aldehyde group, respectively (Figure 1G). Acid-catalyzed deprotection of the acetal in *poly*-**1b** (Figure 1A) leads to the loss of signal at δ = 3.27 ppm along with the emergence of a new resonance at δ = 9.95 ppm corresponding to the second free aldehyde in *poly*-**4b** transferred as part of the initiation step. Integration of the corresponding ^{1}H NMR resonances for *poly*-**1b** samples prepared from $[\mathbf{M}]_0/[\mathbf{I}]_0$ loadings of $20 < [\mathbf{M}]_0/[\mathbf{I}]_0 < 100$ suggest termination efficiencies in excess of 90% (Figure 1B).

Solution-based cyclodehydrogenation of *poly*-4b

We next sought to explore the conversion of solubilized, end-functionalized, and length-controlled samples of *poly*-**4b** into the corresponding 9-AGNRs (Figure 2A). Scholl-type[29–31] cyclodehydrogenation reactions mediated by either $FeCl_3$ or 2,3-dichloro-5,6-dicyano-1,4-benzoquinone (DDQ)/trifluoromethanesulfonic acid (TfOH) as oxidants yielded amorphous precipitates that have commonly been associated with the formation of GNRs (Figure 2A, path A). It is important to highlight here that a structural assignment of cyclodehydrogenation products emerging from Scholl-type reactions in macromolecular systems remains controversial and has largely relied on an assembly of circumstantial evidence based on discrete small-molecule model systems, or ensemble characterization techniques. This realization will be relevant as we proceed in our analysis of the products emerging from *poly*-**4b**. UV-Vis spectroscopy of the sparingly soluble precipitate obtained from in-solution cyclodehydrogenation of *poly*-**4b** ($M_n = 7.8 \times 10^3$ g mol^{-1}) shows a bathochromic shift and broadening of the absorption spectrum suggestive of the transition from a *poly*-(*p*-phenylene) chromophore (λ_{max} = 292 nm) to the expected extended polycyclic aromatic backbone (λ_{max} = 293, 342, 482, 530, and 768 nm) (Figure 2B).[32] Vibrational (IR) spectroscopy (Figure 2C) recorded on both *poly*-**4b** precursors and the corresponding Scholl-type reaction products shows the characteristic alkyl and aryl C–H stretching and bending modes (2,918, 2,848, and 1,456 cm^{-1}, respectively) along with the aldehyde C=O stretching mode at 1,714 cm^{-1}. An increase in the aromatic C=C stretching mode at 1,557 cm^{-1} can be attributed to the expansion of the polycyclic aromatic backbone. Raman spectroscopy reveals the characteristic signature of D and G peaks, 1,320 and 1,598 cm^{-1}, respectively, along with 2D, D + G, and 2G overtones (Figure 2D) commonly observed for extended nanographenes. Curiously, the radial breathing-like mode (RBLM), a distinctive feature observed in samples of on-surface grown 9-AGNRs (RBLM ~ 310–320 cm^{-1}) is absent from the spectrum.[32] This controversy raises renewed concerns regarding the reliance on ensemble characterization tools used in the structural assignment of products emerging from solution-based Scholl-type reactions in bottom-up GNR synthesis.

In an attempt to resolve this paradox, we herein set out to characterize the sparingly soluble products of a Scholl-type oxidation of *poly*-**4b** using cryogenic (4 K) scanning tunneling microscopy (STM) in ultra-high vacuum (UHV). Samples of cyclodehydrogenated *poly*-**4b** dispersed in an inert matrix of pyrene were deposited on Au(111) surfaces using matrix-assisted direct (MAD) transfer techniques.[33] Topographic STM images (Figures 2E and 2H) recorded on samples annealed at 353 K for 12 h to induce lateral diffusion and traceless sublimation of the pyrene matrix show irregular graphitic networks (apparent height 0.20 ± 0.05 nm) that cannot be mapped onto the molecular structure of the 9-AGNR backbone. The discrepancies between ensemble-based characterization, i.e., UV-Vis, IR, Raman, and single-molecule-resolved STM imaging uniquely enabled by MAD transfer techniques echoes the structural complexity emerging from radical cation rearrangements and fragmentation reactions intrinsic to a given polycyclic aromatic hydrocarbon (PAH) scaffold when subjected to Scholl-type reaction conditions. The obvious dissonance between traditional ensemble-based tools and the amorphous graphitic networks emerging from Scholl-type reactions revealed by STM has considerably raised the burden of evidence required to support a claim of in-solution cyclodehydrogenated GNRs.

MAD transfer and surface-assisted cyclodehydrogenation of *poly*-4b

To overcome the technical challenge associated with suppressing undesired side reactions during the Scholl-type oxidation of *poly*-**4a**, we adopted a hybrid GNR growth process. Although SCTP provides us with a high degree of control over the end-functionalization of the 9-AGNR polymer precursor and ready access to low dispersities, MAD transfer followed by surface-assisted cyclodehydrogenation ensures the formation of only the desired C–C bonds that map onto the crystallographic unit cell of the fused GNR backbone. Guided by this idea, we prepared high-dilution samples of low dispersity *poly*-**4a** ($[\mathbf{M}]_0/[\mathbf{I}]_0$ = 20) in a pyrene matrix for MAD transfer onto a clean Au(111) surface held at 297 K (see detailed procedure in the STAR Methods section). Molecule-decorated surfaces were annealed in UHV for 12 h at 353 K to induce the sublimation of the bulk pyrene matrix and diffusion of *poly*-**4a** across the surface. Further annealing at 648 K for 30 min induces a thermal cyclodehydrogenation that leads to the fully fused 9-AGNR backbone. Figure 2I shows a constant-current STM image of a sub-monolayer coverage of 9-AGNR-**4a** on Au(111) at $T = 4$ K. Large-area topographic scans reveal that 9-AGNR-**4a** featuring narrow length distributions ($\bar{l} = 6.42 \pm 0.98 \text{nm}$, inset in Figure 2I) commensurate with the average

DP of *poly*-**4a** derived from SEC (Figure 1B). 9-AGNRs assemble into long-range-ordered domains that align with the elbows of the herring-bone reconstruction of the Au(111) surface. The average lateral spacing between GNRs is >3 nm, precluding any direct interaction between individual ribbons. Higher-resolution constant-current STM images (Figures 2J and S2) reveal GNRs featuring an apparent height and width of 0.19 ± 0.01 and 1.00 ± 0.01 nm, respectively, consistent with the formation of the fully conjugated 9-AGNR backbone. A majority of ribbons feature at least one (>90%) or both (>70%) distinctive end groups, i.e., the 2-bromo-1,1′-biphenyl and the phenylboronic acid (blue and orange phenyl rings in Figures 1A and 2A), transferred as part of the SCTP initiation and termination steps (we will herein use these groups to refer to the initiator end and the terminator end of the 9-AGNR, respectively). Singular indentations along the armchair edges of 9-AGNRs result from a commonly observed phenyl cleavage attributed to the occasional breaking of C–C bonds during the cyclodehydrogenation step (Figure S3B).[34–36] Tip-functionalized bond-resolved STM (BRSTM) images recorded on a representative fully cyclized 9-AGNR-**4a** (*DP* = 15) (Figure 2L) and a shorter ribbon (*DP* = 11) (Figure 2K) show atomically smooth armchair edges along with both end groups transferred during the initiation and termination step. Although BRSTM images reveal the characteristic pattern of four laterally fused benzene rings (i.e., a tetracene core) spanning the width of the 9-AGNR backbone, closer inspection reveals that the thermally labile aldehyde groups lining the ends of *poly*-**4a**, used as diagnostic ^{1}H NMR markers during the SCTP (Figure 1G), are cleaved during the cyclodehydrogenation step. This observation is consistent with MALDI-TOF experiments that only show the mass of the molecular ions $[M]^+$ = [*poly*-**1b**–CHO] (Figure 1F). The robust correlation between solution-based SCTP polymer characterization and the length distribution derived from STM of 9-AGNRs resulting from on-surface cyclodehydrogenation highlights the unrivaled structural control innate to our hybrid SCTP/MAD transfer bottom-up approach.

Scanning tunneling spectroscopy of 9-AGNRs

We herein used differential conductance spectroscopy to explore the local electronic structure of 9-AGNR-**4a** emerging from SCTP polymers. Typical dI/dV point spectra recorded along the armchair edge of a pristine 9-AGNR-**4a** (Figure 3A, positions marked with red crosses in the BRSTM image inset) show four prominent features. A broad peak centered at $V_s = -0.25 \pm 0.05$ V (*Peak* 3) and a sharp signature at $V_s = +1.10 \pm 0.05$ V (*Peak* 4) have previously been assigned to the valence (VB) and conduction band (CB) edges of bulk 9-AGNRs, respectively, giving rise to a band gap of $E_g \sim 1.4$ eV on Au(111).[34–36] The peaks at $V_s = -1.30 \pm 0.05$ V (*Peak* 1) and $V_s = 1.50 \pm 0.05$ V (*Peak* 5) correspond to the VB − 1 and CB + 1, band edges, respectively. dI/dV point spectra recorded near either the initiator (position marked with a blue cross in BRSTM image inset) or the terminator end of the ribbon (position marked with an orange cross in the BRSTM image inset) mirror the bulk VB states but feature one additional low-lying state at $V_s = -0.90 \pm 0.05$ V (*Peak* 2) not observed in 9-AGNRs fabricated through on-surface polymerization and cyclodehydrogenation.[34–36] Differential conductance maps recorded at biases corresponding to *Peak* 5 and *Peak* 4 in the point spectra show the characteristic nodal patterns associated with the CB + 1 and CB lining the armchair edges of the ribbon (Figures 3B and 3C). At negative bias across the range of $-0.20\text{ V} > V_s > -0.30$ V (Figures

3D and 3E) d*I*/d*V* maps are saturated by the Au(111) surface state. Despite the large background signal, Figure 3D shows the distinctive signature of the VB (*Peak* 3)−bright lobes lining the armchair edges contrasted by a dark feature-less GNR backbone. Unique to 9-AGNRs synthesized through our hybrid SCTP/MAD transfer approach is a characteristic signature associated with the functional end groups transferred during the initiation and termination steps of the polymerization. A differential conductance map recorded at V_S = −0.90 V (*Peak* 2) shows three bright lobes lining the lower (initiator) end of the ribbon and two bright spots flanking the cove-type structure lining the upper (terminator) end of the GNR (see arrows in Figure 3F). Rather than invoking a localized filled end state, these unique features are associated with a local broadening of the VB state induced by the termination of the ribbon. The correspondence between the chemical structure of initiator and terminator ends derived from BRSTM and the emergence of distinctive peaks and nodal patterns at discrete energies in differential conductance spectroscopy validates that the chemical design of SCTP initiator and terminator groups seamlessly translate into the functional engineering of electronic states in bottom-up synthesized GNRs. Our hybrid SCTP/MAD transfer process thus not only provides exquisite control over the length, width, and end groups of bottom-up synthesized GNRs but presents an unparalleled tool to access and fine-tune the band alignment and contact resistance at the critical metal-semiconductor interface of nanoribbon device architectures, paving the way for technological advancements in the field of carbon-based nanoelectronics sensing and computing.

EXPERIMENTAL PROCEDURES

Resource availability

Lead contact—Further information and requests for resources should be directed to and will be fulfilled by the lead contact, Prof. Felix Fischer (ffischer@berkeley.edu).

Materials availability—Subject to availability, all stable reagents generated in this study will be made available on request, but we might require a payment and/or a completed materials transfer agreement if there is potential for commercial application.

Data and code availability—The Cartesian coordinates for the crystallographic data reported in this article are included in Data S1. The crystallographic data for 2 reported in this article have been deposited at the Cambridge Crystallographic Data Centre (CCDC) under deposition number CCDC: 2303331. These data can be obtained free of charge from the CCDC at http://www.ccdc.cam.ac.uk/data_request/cif. Other data supporting this study are available in the article and supplemental information.

Synthesis and characterization

Polymer synthesis and GNR growth—Full details of the synthesis and characterization of **1a,b, 2**, as well as polymers *poly*-**1a,b** and *poly*-**4a,b**, are given in the supplemental information. 9-AGNRs were grown from *poly*-**4a** on Au(111)/mica films under UHV conditions. Atomically clean Au(111) surfaces were prepared through iterative Ar^+ sputter/anneal cycles. Sub-monolayer coverage of *poly*-**4a** on atomically clean Au(111) was obtained by MAD transfer. *poly*-**4a** was dispersed in molten pyrene (pyrene:*poly*-**4a** =

5,000:1 w/w) under an inert atmosphere and flash frozen at 77 K. The glassy solid was ground to a fine powder and sprinkled onto an atomically clean Au(111) substrate in ambient air at $T = 298$ K. The sample was transferred into UHV ($p < 10^{-9}$ Pa) and annealed at $T = 353$ K for $t \sim 12$ h to induce the slow sublimation of pyrene and diffusion of polymers across the surface. The surface temperature was slowly ramped ($\leq$ 2 K min^{-1}) to 648 K and held at this temperature for 30 min to induce the radical-step growth polymerization and on-surface cyclodehydrogenation. MAD transfer samples of 9-AGNR-**4b** and 9-AGNR-**4b** resulting from Scholl-type oxidative cyclodehydrogenation in solution were prepared following the same procedure.

STM characterization—All STM experiments were performed using a commercial OMICRON LT-STM held at $T = 4$ K using PtIr STM tips. STM tips were optimized for scanning tunneling spectroscopy using an automated tip conditioning program.[37] $\mathrm{d}I/\mathrm{d}V$ measurements were recorded with CO-functionalized STM tips using a lock-in amplifier with a modulation frequency of 455 Hz and a modulation amplitude of $V_{\mathrm{RMS}} = 10$ mV. $\mathrm{d}I/\mathrm{d}V$ point spectra were recorded under open feedback loop conditions. $\mathrm{d}I/\mathrm{d}V$ maps were collected under constant current conditions. BRSTM images were obtained by mapping the out-of-phase $\mathrm{d}I/\mathrm{d}V$ signal collected during a constant-height $\mathrm{d}I/\mathrm{d}V$ map at 10 mV. Peak positions in $\mathrm{d}I/\mathrm{d}V$ point spectroscopy were determined by fitting the spectra with Lorentzian peaks. Each peak position is based on an average of ~10 spectra collected on various GNRs with different tips, all of which were first calibrated to the Au(111) Shockley surface state.

Supplementary Material

Refer to Web version on PubMed Central for supplementary material.

ACKNOWLEDGMENTS

This work was primarily funded by the U.S. Department of Energy (DOE), Office of Science, Basic Energy Sciences (BES), and Materials Sciences and Engineering Division under contract no. DE-AC02-05-CH11231 (Nanomachine program KC1203) (molecular design, catalyst development, and polymer synthesis) and contract no. DE-SC0023105 (surface growth). STM characterization was supported by the U.S. Department of Defense (DOD), Office of Naval Research (ONR) under award no. N00014-19-1-2503 and STS analysis by the National Science Foundation (NSF) under award no. CHE-2203911. Part of this research program was generously supported by the Heising-Simons Faculty Fellows Program at UC Berkeley. STM instruments are supported in part by the U.S. Department of Defense (DOD), Office of Naval Research (ONR) under award no. N00014-20-1-2824. The authors thank the College of Chemistry (CoC) for use of resources at their NMR and small-molecule X-ray crystallography facility. The authors thank their staff Hasan Çelik and Nicholas Settineri for assistance. Instruments in CoC-NMR facility are supported in part by NIH S10-OD024998. Instruments in CoC-X-ray facility are supported in part by NIH S10-RR027172.

REFERENCES

1. Yoon KY, and Dong GB (2020). Liquid-phase bottom-up synthesis of graphene nanoribbons. Mater. Chem. Front. 4, 29–45.
2. Wu JS, Gherghel L, Watson MD, Li JX, Wang ZH, Simpson CD, Kolb U, and Müllen K. (2003). From branched polyphenylenes to graphite ribbons. Macromolecules 36, 7082–7089.
3. Narita A, Feng XL, Hernandez Y, Jensen SA, Bonn M, Yang HF, Verzhbitskiy IA, Casiraghi C, Hansen MR, Koch AHR, et al. (2014). Synthesis of structurally well-defined and liquid-phase-processable graphene nanoribbons. Nat. Chem. 6, 126–132. [PubMed: 24451588]

4. Narita A, Verzhbitskiy IA, Frederickx W, Mali KS, Jensen SA, Hansen MR, Bonn M, De Feyter S, Casiraghi C, Feng X, et al. (2014). Bottom-up synthesis of liquid-phase-processable graphene nanoribbons with near-infrared absorption. ACS Nano 8, 11622–11630. [PubMed: 25338208]
5. Yang XY, Dou X, Rouhanipour A, Zhi LJ, Rä der HJ, and Müllen K. (2008). Two-dimensional graphene nanoribbons. J. Am. Chem. Soc. 130, 4216–4217. [PubMed: 18324813]
6. Schwab MG, Narita A, Osella S, Hu YB, Maghsoumi A, Mavrinsky A, Pisula W, Castiglioni C, Tommasini M, Beljonne D, et al. (2015). Bottom-up synthesis of necklace-like graphene nanoribbons. Chem. Asian J. 10, 2134–2138. [PubMed: 26062724]
7. Li G, Yoon KY, Zhong XJ, Zhu XY, and Dong GB (2016). Efficient bottom-up preparation of graphene nanoribbons by mild Suzuki-Miyaura polymerization of simple triaryl monomers. Chemistry 22, 9116–9120. [PubMed: 27159538]
8. Li G, Yoon KY, Zhong XJ, Wang JC, Zhang R, Guest JR, Wen JG, Zhu XY, and Dong GB (2018). A modular synthetic approach for band-gap engineering of armchair graphene nanoribbons. Nat. Commun. 9, 1687. [PubMed: 29703958]
9. Yin JL, Jacobse PH, Pyle D, Wang ZY, Crommie MF, and Dong GB (2022). Programmable fabrication of monodisperse graphene nanoribbons via deterministic iterative synthesis. J. Am. Chem. Soc. 144, 16012–16019. [PubMed: 36017775]
10. Schwab MG, Narita A, Hernandez Y, Balandina T, Mali KS, De Feyter S, Feng XL, and Müllen K. (2012). Structurally defined graphene nanoribbons with high lateral extension. J. Am. Chem. Soc. 134, 18169–18172. [PubMed: 23082776]
11. Jänsch D, Ivanov I, Zagranyarski Y, Duznovic I, Baumgarten M, Turchinovich D, Li C, Bonn M, and Müllen K. (2017). Ultranarrow low-bandgap graphene nanoribbons from Bromoperylenes—synthesis and terahertz-spectroscopy. Chemistry 23, 4870–4875. [PubMed: 28318065]
12. Cai JM, Ruffieux P, Jaafar R, Bieri M, Braun T, Blankenburg S, Muoth M, Seitsonen AP, Saleh M, Feng XL, et al. (2010). Atomically precise bottom-up fabrication of graphene nanoribbons. Nature 466, 470–473. [PubMed: 20651687]
13. Ruffieux P, Wang SY, Yang B, Sánchez-Sánchez C, Liu J, Dienel T, Talirz L, Shinde P, Pignedoli CA, Passerone D, et al. (2016). On-surface synthesis of graphene nanoribbons with zigzag edge topology. Nature 531, 489–492. [PubMed: 27008967]
14. Rizzo DJ, Veber G, Cao T, Bronner C, Chen T, Zhao FZ, Rodriguez H, Louie SG, Crommie MF, and Fischer FR (2018). Topological band engineering of graphene nanoribbons. Nature 560, 204–208. [PubMed: 30089918]
15. Gröning O, Wang SY, Yao XL, Pignedoli CA, Borin Barin GB, Daniels C, Cupo A, Meunier V, Feng XL, Narita A, et al. (2018). Engineering of robust topological quantum phases in graphene nanoribbons. Nature 560, 209–213. [PubMed: 30089919]
16. Yokoyama A, Suzuki H, Kubota Y, Ohuchi K, Higashimura H, and Yokozawa T. (2007). Chain-growth polymerization for the synthesis of polyfluorene via Suzuki-Miyaura coupling reaction from an externally added initiator unit. J. Am. Chem. Soc. 129, 7236–7237. [PubMed: 17506555]
17. Yokozawa T, and Yokoyama A. (2009). Chain-growth condensation polymerization for the synthesis of well-defined condensation polymers and pi-conjugated polymers. Chem. Rev. 109, 5595–5619. [PubMed: 19757808]
18. Elmalem E, Kiriy A, and Huck WTS (2011). Chain-growth Suzuki polymerization of n-type fluorene copolymers. Macromolecules 44, 9057–9061.
19. Zhang HH, Xing CH, and Hu QS (2012). Controlled Pd(0)/t-Bu3P-catalyzed Suzuki cross-coupling polymerization of AB-type monomers with PhPd(t-Bu3P)I or Pd2(dba)3/t-Bu3P/Arl as the initiator. J. Am. Chem. Soc. 134, 13156–13159. [PubMed: 22860802]
20. Elmalem E, Biedermann F, Johnson K, Friend RH, and Huck WTS (2012). Synthesis and photophysics of fully pi-conjugated heterobis-functionalized polymeric molecular wires via Suzuki chain-growth polymerization. J. Am. Chem. Soc. 134, 17769–17777. [PubMed: 23020174]
21. Zhang HH, Xing CH, Hu QS, and Hong KL (2015). Controlled Pd(0)/t-Bu3P-catalyzed Suzuki cross-coupling polymerization of AB-type monomers with ArPd(t-Bu3P)X or Pd2(dba)3/t-Bu3P/ArX as the initiator. Macromolecules 48, 967–978.
22. Zhang HH, Hu QS, and Hong K. (2015). Accessing conjugated polymers with precisely controlled heterobisfunctional chain ends via post-polymerization modification of the OTf group

and controlled Pd(0)/t-Bu3P-catalyzed Suzuki cross-coupling polymerization. Chem. Commun. (Camb) 51, 14869–14872. [PubMed: 26299669]

23. Dong J, Guo H, and Hu QS (2017). Controlled Pd(0)/Ad3P-catalyzed Suzuki cross-coupling polymerization of AB-type monomers with Ad_3P-coordinated acetanilide-based palladacycle complex as initiator. ACS Macro Lett. 6, 1301–1304. [PubMed: 35650786]

24. Seo KB, Lee IH, Lee J, Choi I, and Choi TL (2018). A rational design of highly controlled Suzuki-Miyaura catalyst-transfer polycondensation for precision synthesis of polythiophenes and their block copolymers: marriage of palladacycle precatalysts with MIDA-boronates. J. Am. Chem. Soc. 140, 4335–4343. [PubMed: 29522325]

25. Lee J, Kim H, Park H, Kim T, Hwang SH, Seo D, Chung TD, and Choi TL (2021). Universal Suzuki-Miyaura catalyst-transfer polymerization for precision synthesis of strong donor/acceptor-based conjugated polymers and their sequence engineering. J. Am. Chem. Soc. 143, 11180–11190. [PubMed: 34264077]

26. Kim H, Lee J, Kim T, Cho M, and Choi TL (2022). Precision synthesis of various low-bandgap donor-acceptor alternating conjugated polymers via living Suzuki-Miyaura catalyst-transfer polymerization. Angew. Chem. Int. Ed. Engl. 61, e202205828.

27. Park H, Lee J, Hwang SH, Kim D, Hong SH, and Choi TL (2022). Modulating the rate of controlled Suzuki-Miyaura catalyst-transfer polymerization by boronate tuning. Macromolecules 55, 3476–3483.

28. Lee JH, Ryu H, Park S, Cho MY, and Choi TL (2023). Living Suzuki-Miyaura catalyst-transfer polymerization for precision synthesis of length-controlled armchair graphene nanoribbons and their block copolymers. J. Am. Chem. Soc. 145, 15488–15495. [PubMed: 37376993]

29. Grzybowski M, Skonieczny K, Butenschön H, and Gryko DT (2013). Comparison of oxidative aromatic coupling and the Scholl reaction. Angew. Chem. Int. Ed. Engl. 52, 9900–9930. [PubMed: 23852649]

30. Zhang YQ, Pun SH, and Miao Q. (2022). The Scholl reaction as a powerful tool for synthesis of curved polycyclic aromatics. Chem. Rev. 122, 14554–14593. [PubMed: 35960873]

31. Veber G, Diercks CS, Rogers C, Perkins WS, Ciston J, Lee K, Llinas JP, Liebman-Peláez A, Zhu CH, Bokor J, et al. (2020). Reticular growth of graphene nanoribbon 2D covalent organic frameworks. Chem 6, 1125–1133.

32. Borin Barin GB, Fairbrother A, Rotach L, Bayle M, Paillet M, Liang LB, Meunier V, Hauert R, Dumslaff T, Narita A, et al. (2019). Surface-synthesized graphene nanoribbons for room temperature switching devices: substrate transfer and ex situ characterization. ACS Appl. Nano Mater. 2, 2184–2192.

33. McCurdy RD, Jacobse PH, Piskun I, Veber GC, Rizzo DJ, Zuzak R, Mutlu Z, Bokor J, Crommie MF, and Fischer FR (2021). Synergetic bottom-up synthesis of graphene nanoribbons by matrix-assisted direct transfer. J. Am. Chem. Soc. 143, 4174–4178. [PubMed: 33710887]

34. Talirz L, Söde H, Dumslaff T, Wang SY, Sanchez-Valencia JR, Liu J, Shinde P, Pignedoli CA, Liang LB, Meunier V, et al. (2017). On-surface synthesis and characterization of 9-atom wide armchair graphene nanoribbons. ACS Nano 11, 1380–1388. [PubMed: 28129507]

35. Rizzo DJ, Jiang J, Joshi D, Veber G, Bronner C, Durr RA, Jacobse PH, Cao T, Kalayjian A, Rodriguez H, et al. (2021). Rationally designed topological quantum dots in bottom-up graphene nanoribbons. ACS Nano 15, 20633–20642. [PubMed: 34842409]

36. Merino-Díez N, Garcia-Lekue A, Carbonell-Sanromà E, Li JC, Corso M, Colazzo L, Sedona F, Sánchez-Portal D, Pascual JI, and de Oteyza DG (2017). Width-dependent band gap in armchair graphene nanoribbons reveals Fermi level pinning on Au(111). ACS Nano 11, 11661–11668. [PubMed: 29049879]

37. Wang SK, Zhu JM, Blackwell R, and Fischer FR (2021). Automated tip conditioning for scanning tunneling spectroscopy. J. Phys. Chem. A 125, 1384–1390. [PubMed: 33560124]

Highlights

Bottom-up synthesis of graphene nanoribbons (GNRs) from polymer precursors

Living catalyst-transfer polymerization controls GNR length, width, and end groups

Surface-assisted cyclodehydrogenation of polymers gives rise to GNRs

THE BIGGER PICTURE

The unusual electronic structure of graphene nanoribbons (GNRs) emerges from quantum confinement effects imposed by their widths, lengths, and edge structures. Exercising concurrent control over these key parameters using chemical bottom-up synthesis techniques has remained a challenge in current GNR technologies. In this study, we present a hybrid approach that merges catalyst-transfer polymerization and surface-assisted cyclodehydrogenation protocols that together enable precise control over GNR length, width, and end groups.

It is these structural parameters that have given rise to highly tunable semiconductors, innate metallicity arising from topological zero-mode engineering, or magnetic ordering in spin-polarized lattices. The uncompromising control over GNR structure, and its tightly linked electronic properties, thus provides a universal and modular platform for the systematic exploration and seamless integration of functional GNRs with integrated circuit architectures.

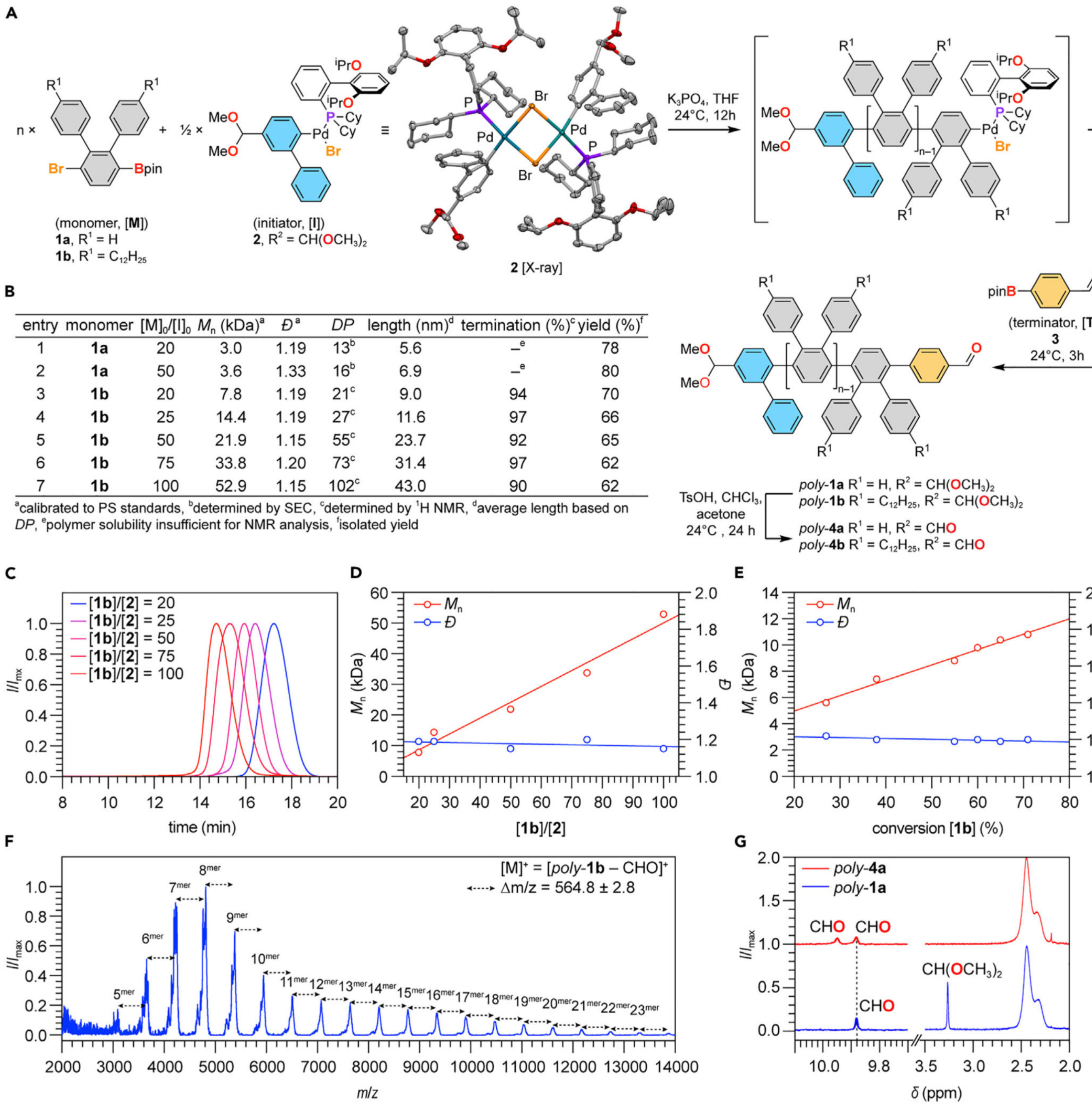

entry	monomer	$[M]_0/[I]_0$	M_n (kDa)[a]	$Đ$[a]	*DP*	length (nm)[d]	termination (%)[c]	yield (%)[f]
1	**1a**	20	3.0	1.19	13[b]	5.6	–[e]	78
2	**1a**	50	3.6	1.33	16[b]	6.9	–[e]	80
3	**1b**	20	7.8	1.19	21[c]	9.0	94	70
4	**1b**	25	14.4	1.19	27[c]	11.6	97	66
5	**1b**	50	21.9	1.15	55[c]	23.7	92	65
6	**1b**	75	33.8	1.20	73[c]	31.4	97	62
7	**1b**	100	52.9	1.15	102[c]	43.0	90	62

[a]calibrated to PS standards, [b]determined by SEC, [c]determined by ^1H NMR, [d]average length based on *DP*, [e]polymer solubility insufficient for NMR analysis, [f]isolated yield

Figure 1. Controlled living Suzuki catalyst-transfer polymerization

(A) Schematic representation of the living SCTP of *o*-terphenylene monomers **1a,b** [**M**] initiated by a Pd(RuPhos) aryl bromide complex **2** [**I**]. The reaction is terminated by a monofunctional boronic acid **3** [**T**]. Single X-ray crystal structure of **2**. Thermal ellipsoids are drawn at the 50% probability level. Color coding: C (gray), O (red), P (purple), Br (orange), and Pd (turquoise). H-atoms are omitted for clarity.

(B) Summary of SEC data, estimated length, termination efficiency, and isolated yields of *poly*-**1a,b** as a function of initial loading $[M]_0/[I]_0$.

(C) SEC traces of *poly*-**1b** samples obtained from various $[M]_0/[I]_0$ loadings.

(D) Linear correlation between M_n and $[M]_0/[I]_0$. $Đ$ remains constant for different $[M]_0/[I]_0$.

(E) Evolution of M_n and β as a function of monomer conversion.

(F) MALDI of *poly*-**1b** ($[M]_0/[I]_0 = 20$) showing a family of polymers separated by the mass of the monomer unit $\Delta m/z$. The molecular ion peaks correspond to the mass of the polymer minus the labile aldehyde group.

(G) ^{1}H-NMR of *poly*-**1b** (blue) and *poly*-**4b** (red). Deprotection of the dimethyl acetal (δ = 3.27 ppm) leads to the emergence of a resonance at δ = 9.95 ppm associated with the second aldehyde group.

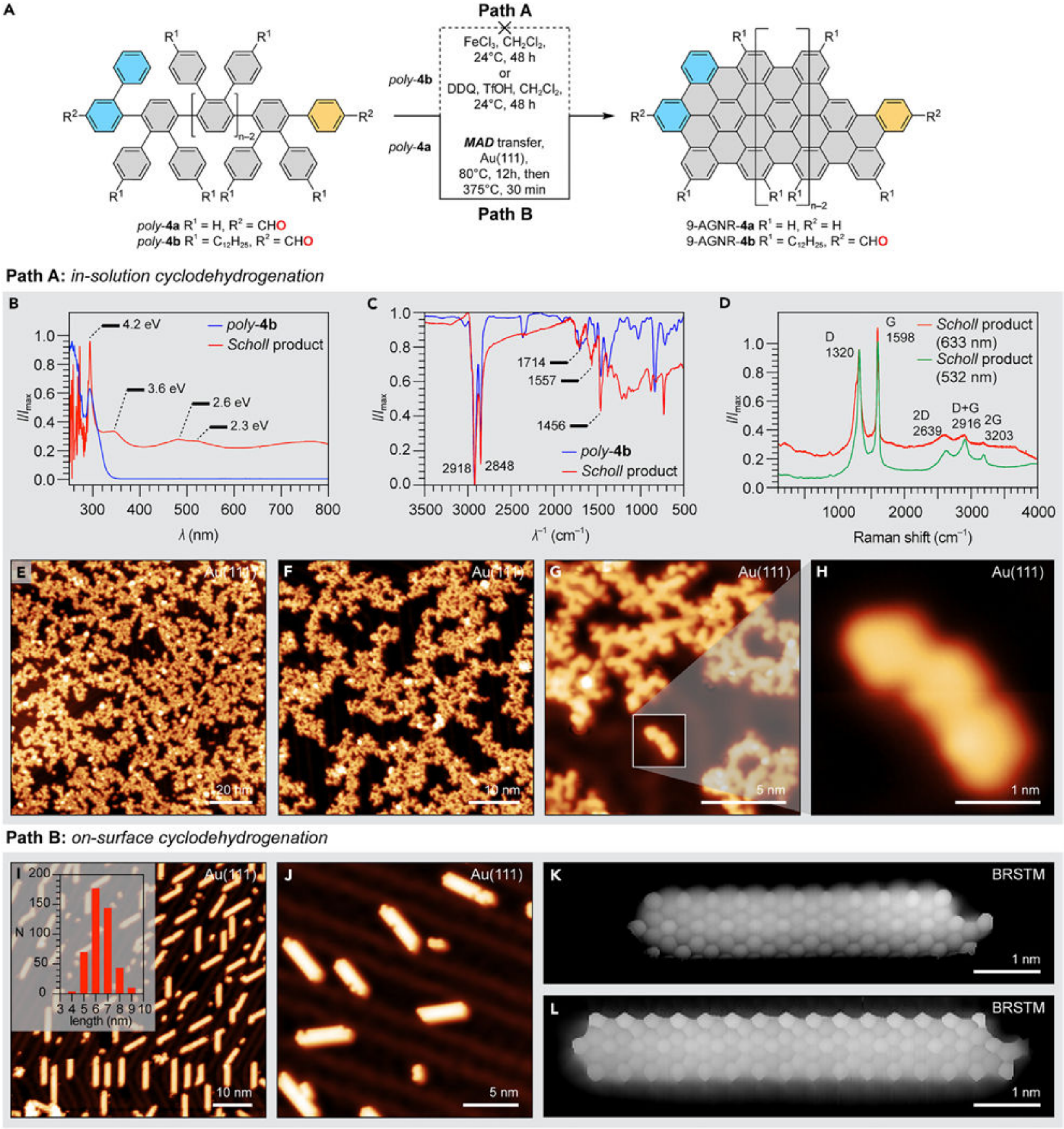

Figure 2. Solution-based cyclodehydrogenation and hybrid surface-assisted synthesis of 9-AGNRs from polymer precursors

(A) Schematic representation of the solution-based Scholl-type reaction of *poly*-**4a** and *poly*-**4b** (path A) and surface-assisted cyclodehydrogenation of *poly*-**4a** on Au(111) (path B).

(B) UV-Vis spectra of *poly*-**4b** and the resulting products following solution-based oxidative cyclodehydrogenation (Scholl-type reaction).

(C) IR spectra of *poly*-**4b** and the resulting products following solution-based oxidative cyclodehydrogenation (Scholl-type reaction).

(D) Raman spectrum of products resulting from solution-based oxidative cyclodehydrogenation (Scholl-type reaction) of *poly*-**4b**. Excitation laser: 633 and 532 nm (spectra are offset for clarity).

(E and F) Large-area topographic STM images (constant current) of MAD transferred annealed samples of 9-AGNR-**4b** cyclodehydrogenated in solution using Scholl or DDQ/TfOH reaction conditions on Au(111) (V_s = 200 mV, I_t = 20 pA).

(G and H) Representative topographic STM images (constant current) of MAD transferred samples of solution cyclodehydrogenated 9-AGNR-**4b** on Au(111) showing a high concentration of structural defects and an internal bonding that cannot be mapped onto the structure of the 9-AGNR backbone (V_s = 200 mV, I_t = 20 pA).

(I) Large-area topographic STM image (constant current) of a MAD transferred annealed sample of *poly*-**4a** ([**M**]$_0$/[**I**]$_0$ = 20) on Au(111) (V_s = 100 mV, I_t = 20 pA). Inset: statistical length distribution of 9-AGNR-**4a** grown on Au(111) from *poly*-**4a** ([**M**]$_0$/[**I**]$_0$ = 20) using the hybrid SCTP/surface-assisted cyclodehydrogenation approach; $l - = 6.42$nm, $\mu_{1/2}$ = 6 nm, σ = 0.98 nm.

(J) Topographic STM image (constant current) of a MAD transferred annealed sample of *poly*-**4a** ([**M**]$_0$/[**I**]$_0$ = 20) on Au(111) (V_s = 50 mV, I_t = 20 pA).

(K and L) BRSTM images (constant height) of a pristine 9-AGNR-**4a** (DP = 11 and 15) grown on Au(111) from *poly*-**4a** ([M]$_0$/[I]$_0$ = 20) using the hybrid SCTP/surface-assisted cyclodehydrogenation approach (V_s = 10 mV, V_{ac} = 10 mV, f = 455 Hz, CO-functionalized tip). All STM experiments performed at T =4 K.

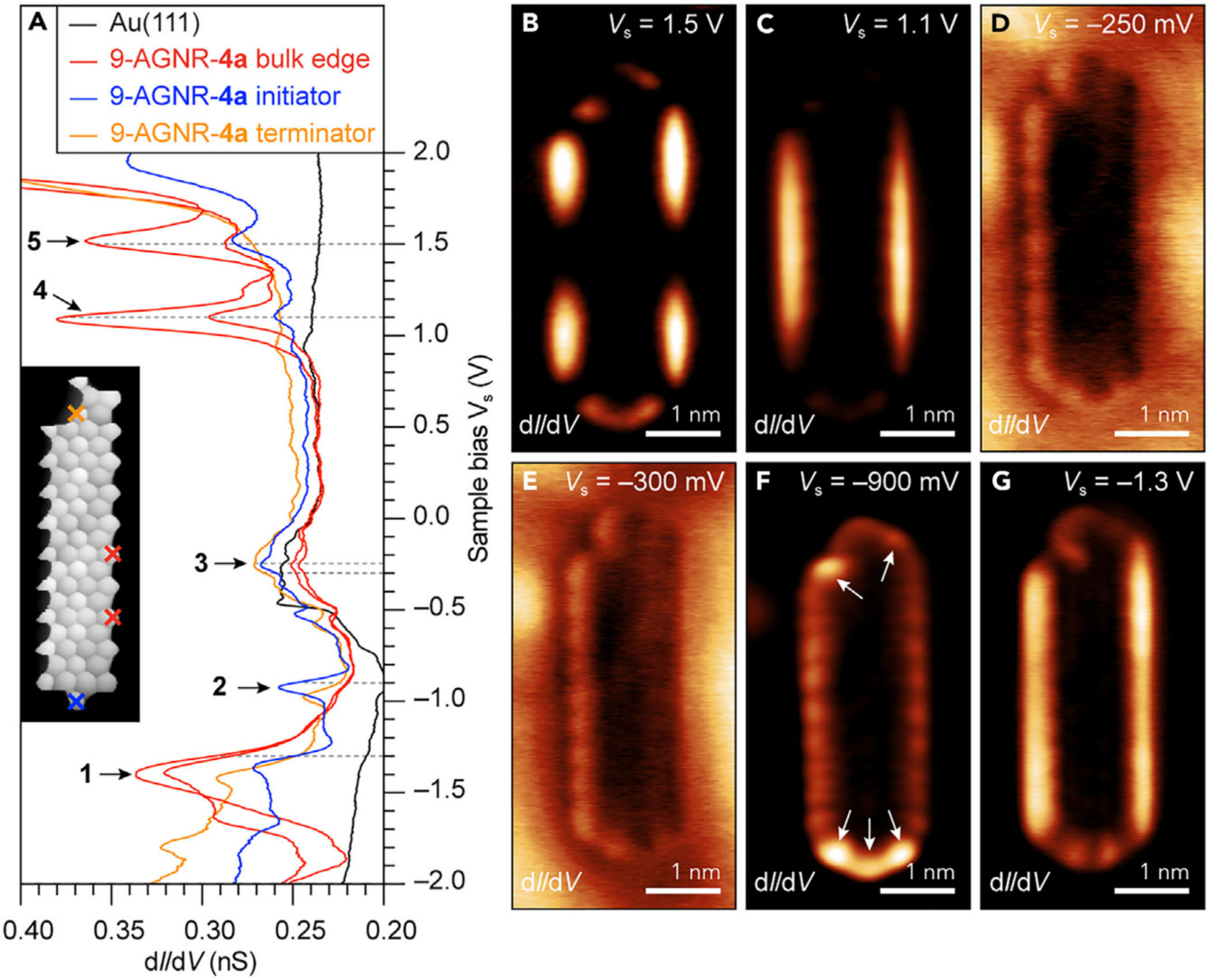

Figure 3. Electronic structure and differential conductance maps of end-functionalized 9-AGNRs

(A) dI/dV point spectra of a 9-AGNR-**4a** on Au(111) recorded at the position marked in the BRSTM inset (Au(111) surface state, black; armchair edge, red; initiator end, blue; terminator end, orange; V_{ac} = 10 mV, f = 455 Hz, CO-functionalized tip).

(B–G) Differential conductance maps (dI/dV) recorded at the highlighted bias voltages (V_s) on a 9-AGNR-**4a** (DP = 9) shown in the inset of (A).